ACS Partner Journal

Journal of the American Society for Mass Spectrometry

pubs.acs.org/jasms

Article

Accumulation of Large Ion Populations with High Ion Densities and Effects Due to Space Charge in Traveling Wave-Based Structures for Lossless Ion Manipulations (SLIM) IMS-MS

Pearl Kwantwi-Barima, Sandilya V. B. Garimella, Isaac K. Attah, Xueyun Zheng, Yehia M. Ibrahim, and Richard D. Smith*

Cite This: J. Am. Soc. Mass Spectrom. 2024, 35, 365−377

Read Online

ACCESS | Metrics & More | Article Recommendations | Supporting Information

ABSTRACT: The accumulation of very large ion populations in traveling wave (TW)-based Structures for Lossless ion Manipulations (SLIM) has been studied to better understand aspects of "in-SLIM" ion accumulation, and particularly its use in conjunction with ion mobility spectrometry (IMS). A linear SLIM ion path was implemented that had a "gate" for blocking and accumulating ions for arbitrary time periods. Removing the gate potential caused ions to exit, and the spatial distributions of accumulated ions examined. The ion populations for a set of peptides increased approximately linearly with increased accumulation times until space change effects became significant, after which the peptide precursor ion populations decreased due to growing space charge-related ion activation, reactions, and losses. Ion activation increased with added storage times and the TW amplitude. Lower amplitude TWs in the accumulation/storage region prevented or minimized ion losses or ion heating effects that can also lead to fragmentation. Our results supported the use of an accumulation region close to the SLIM entrance for speeding accumulation, minimizing ion heating, and avoiding ion population profiles that result in IMS peak tailing. Importantly, space charge-driven separations were observed for large populations of accumulated species and attributed to the opposing effects of space charge and the TW. In these separations, ion species form distributions or peaks, sometimes moving against the TW, and are ordered in the SLIM based on their mobilities. Only the highest mobility ions located closest to the gate in the trapped ion population (and where the highest ion densities were achieved) were significantly activated. The observed separations may offer utility for ion prefractionation of ions and increasing the dynamic range measurements, increasing the resolving power of IMS separations by decreasing peak widths for accumulated ion populations, and other purposes benefiting from separations of extremely large ion populations.

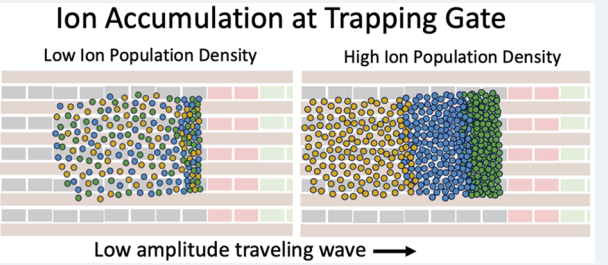

INTRODUCTION

Ion mobility spectrometry (IMS) separates different ion species based on their gas-phase ion mobilities in an electric field,[1−4] and is widely deployed for security screening,[5,6] chemical warfare agent detection,[7−9] and environmental applications.[10,11] IMS coupled with mass spectrometry (IMS-MS) is increasingly important for proteomics and metabolomics,[12−15] and a particularly versatile tool due to its utility for e.g., identification of lipids[16,17] or glycans,[18,19] as well as protein structure studies.[14,20] IMS technologies with distinctive capabilities include drift tube ion mobility (DTIMS),[21,22] differential mobility analysis (DMA),[23,24] high-field asymmetric ion mobility spectrometry (FAIMS),[25,26] trapped ion mobility spectrometry (TIMS),[27,28] and traveling wave ion mobility spectrometry (TWIMS).[29,30] In practice, the performance of DTIMS, for example, is limited by factors that include the drift tube length, introduced ion pulse width, electric field homogeneity, and Coulombic repulsion (i.e., space charge related processes).[31] The utility of IMS in many analytical applications depends significantly on the resolving power (R_p) of separations and the sensitivity of measurements, with the latter being dependent on the size of the ion population that can be utilized for the separation.

Structures for Lossless Ion Manipulations (SLIM)-based TWIMS have enabled ultrahigh R_p separations using extended separation path lengths.[32−34] SLIM TWIMS uses radio frequency (RF) fields in conjunction with direct current (DC) potentials for ion confinement and electric traveling waves (TW) to drive the ion motion. Key features of SLIM, such as moving ions through turns with negligible loss of either R_p or ions,[35] have enabled separations over long serpentine

Received: November 7, 2023
Revised: November 19, 2023
Accepted: December 13, 2023
Published: January 4, 2024

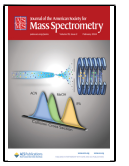

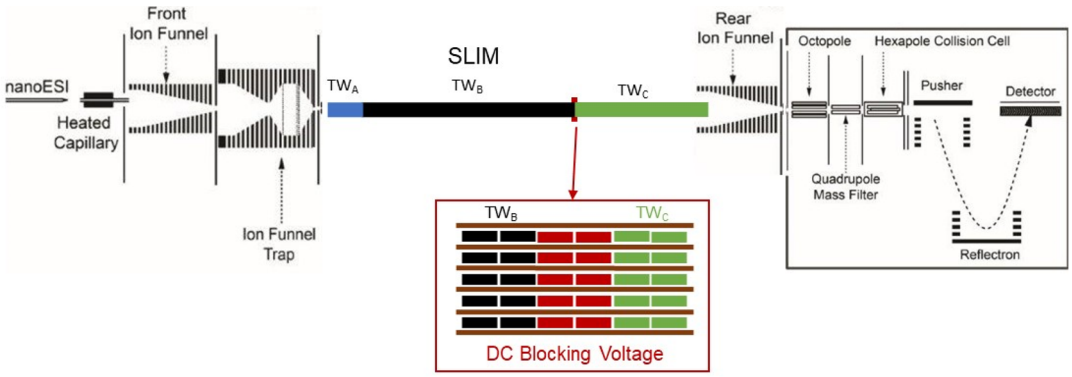

Figure 1. Schematic diagram of the SLIM TWIMS-MS platform and the SLIM module arrangement, having three independently controllable TW regions. The red electrodes indicate the location of the gate that can be provided with a DC blocking potential at the end of region B. The ion funnel trap (IFT) was used to either direct ions from an ESI source into the SLIM or to stop ion accumulation.

paths,[34] with multipass implementations providing unprecedented ultrahigh R_p IMS separations.[36]

However, increasing the IMS R_p using longer path lengths results in longer separation times. Since commonly used electrospray ionization (ESI) sources typically generate ions continuously, most ions generated are not utilized due to ion (charge) capacity limitations of, e.g., an ion funnel trap (IFT), and are effectively discarded. This results in a low overall ion utilization efficiency, particularly for higher R_p SLIM separations and where the size of the starting population constrains measurement sensitivity. This can be further aggravated by efforts to increase R_p by using ion populations of minimal peak width (i.e., very compact).[37] IMS separations (e.g., using drift tubes) with MS often have time scales of 10 to 100 ms and typically use a "pulse" of ions having a temporal width profile of ~1 ms or less in order to maximize R_p.[38] Many approaches for increasing the size of ion populations for injection to lower pressure IMS platforms used in conjunction with MS, such as SLIM, involve the accumulation of ions for some period in a trapping volume.[39,40] While gains can be achieved, such as by using an IFT,[41,42] such approaches are ultimately limited due to charge capacity limitations of the fixed volume of the device. For example, the maximum charge capacity of the IFT is about $\sim 2 \times 10^7$ charges, but $\sim 5 \times 10^6$ charges are typically used to minimize space charge effects that include ion losses, activation (i.e., ion heating), and fragmentation that can degrade analytical utility.[43]

For the long SLIM serpentine ion path arrangements the separations occur over extended times; typically ~0.1 to 1 s, and in some cases >20 s for "multipass" separations.[34] Such separations generally benefit from the use of significantly larger ion accumulation volumes due to the reduced contribution of the initial ion distribution profile; however, overall separation ion utilization efficiencies using a IFT with a continuous ESI source are typically <1%, depending on the details of the ESI-MS interface design.[36] The use of significantly increased ion populations with SLIM TWIMS has been demonstrated,[39] particularly using "in-SLIM" ion accumulation,[44,45] which has been shown to allow $>10^9$ charges to be utilized, orders of magnitude larger than generally employed. Nevertheless, doing this in a manner that optimizes both ion utilization efficiency while not excessively reducing IMS performance (particularly R_p) or causing other undesired effects due to excessive space charge, such as ion heating, remains a challenge.

While there have been several studies on the role of Coulombic ion−ion repulsion and space charge in IMS,[46−52] these previous works have almost exclusively involved space charge effects during mobility separations. These efforts have specifically focused on the distortions in peak shapes and the expansion of peak widths that can occur due to charge−charge interactions for ion population densities significantly below the maximum feasible due to space charge. Space charge effects have been almost always considered problematic: preferably avoided or at least minimized. Indeed, space charge phenomena associated with ion accumulation, trapping, and storage have not been well-studied, particularly for space charge- and ion-density-limited situations relevant to IMS. We also note that computational studies (e.g., ion simulations) in this regime are particularly challenging. This is especially the case for the complex ion confinement fields with SLIM, and for very large ion populations, extreme ion densities, and extended storage times, where space charge effects will be more significant.

Here we report a study of in-SLIM ion accumulation and effects arising from the accumulation of extremely large ion populations with ion densities that become limited by space charge. We discuss the potential of these phenomena for improving IMS applications and other applications by using large ion populations. In this work, we have examined situations where space charge effects can be much greater than typically encountered, providing insights on the ability to accumulate and store ions for greatly extended periods in arbitrarily large volumes. Of particular significance, we present data showing that significant space charge-driven ion separations can occur due to mobility differences for large ion populations with high ion densities, with the highest mobility species driven by the TW accumulating closest to the ion "gate" (blocking voltage). We also find that extended ion accumulation times can lead to significant ion heating (i.e., activation) due to excessive charge density and that ion heating appears to occur only when the region of highest ion densities is close to the space charge limit and thus for the highest mobility species that tend to occupy this region. Finally, we discuss the potential of these phenomena for improving IMS applications and other applications using large ion populations.

EXPERIMENTAL SECTION

Chemicals and Reagents. The peptides Angiotensin II, Kemptide, and Neurotensin used in this study were purchased from Sigma-Aldrich Chemical Co. (Milwaukee, WI, USA) and

https://doi.org/10.1021/jasms.3c00389
J. Am. Soc. Mass Spectrom. 2024, 35, 365−377

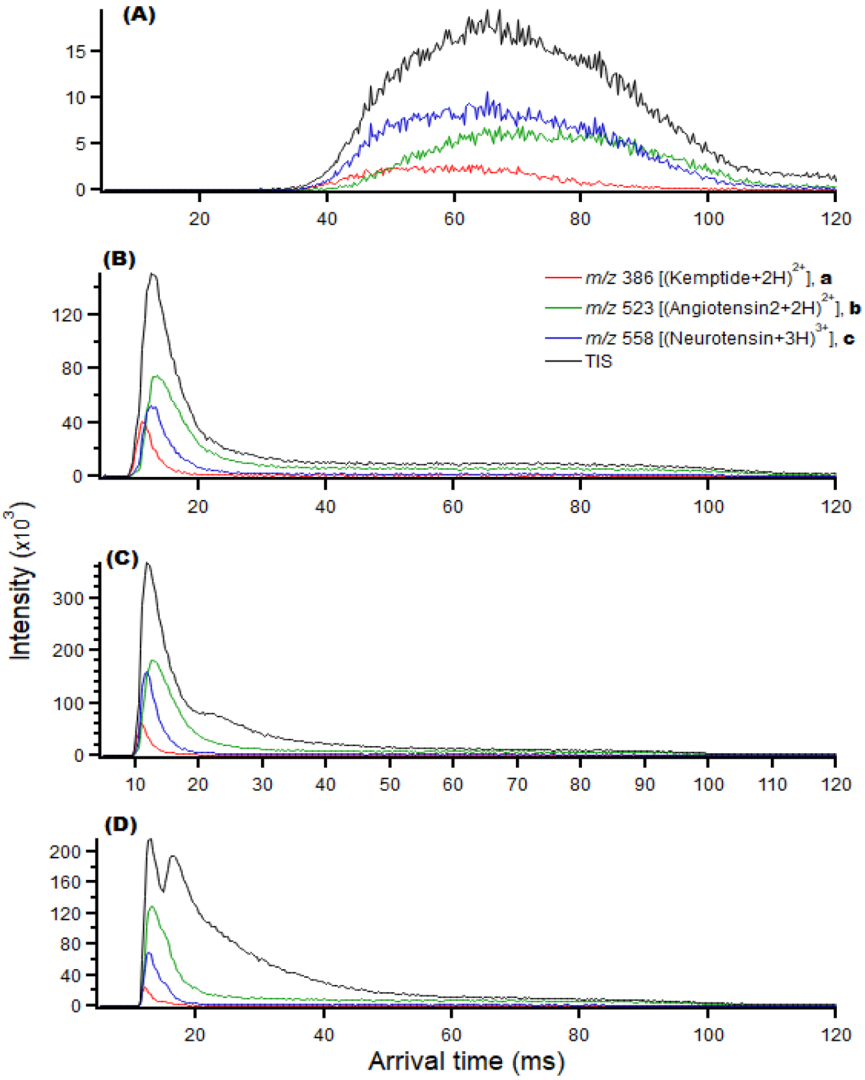

Figure 2. Arrival time distributions (ATD) for the three peptide precursor ions (at m/z 386, 523, and 558; peaks a-c in Figure 3) and the total ion signals (TIS) for ion accumulation times of (A) 49 ms, (B) 163 ms, (C) 326 ms, and (D) 652 ms using 8 $V_{p\text{-}p}$ amplitude TW. Ions in (A) have insufficient time to reach the gate at the end of region B (see Figure 1); ions in (B)−(D) have peaks due to accumulating close to the gate, with long "tails" yet to reach the gate vicinity. See also Figure 3 for the corresponding full mass spectra.

prepared as a mixture at a total solution concentration of 3 μM in 80/20 HPLC grade methanol/water with 0.1% formic acid.

ESI-SLIM TWIMS-MS Instrumentation. A schematic diagram of the instrumentation is shown in Figure 1. A syringe pump flow rate of 0.3 μL/min was used for ESI with a heated inlet capillary maintained at 130 C. Ions were focused through a high-pressure ion funnel (230 $V_{p\text{-}p,}$ 9.40 Torr) and transmitted into the IFT (~230 $V_{p\text{-}p,}$ 2.90 Torr). The IFT was only used for transmitting or blocking the transmission of ions to the SLIM, not for trapping ions. Ion introduction to the SLIM was turned "off" or 'on" using the IFT grids, and ions are were introduced continually from the ion source during the accumulation event period. The ions transmitted to the entrance of the SLIM (at a slightly higher pressure; 2.97 Torr of high-purity nitrogen), where the SLIM TW, RF, and DC potentials guided ions along a linear 45.8 cm path. Ions exiting the SLIM device were transmitted through a rear ion funnel (9.8 V/cm; ~150 $V_{p\text{-}p}$; 0.9 MHz) and RF ion guides to a quadrupole time-of-flight mass spectrometer (QTOF MS; Agilent Technologies model 6538, Santa Clara CA, USA). The DC guard voltage (4 V) and RF potentials (270 $V_{p\text{-}p}$, 1.0 MHz) were used for ion confinement in the SLIM. The TW electrode potentials were generated with a custom power supply described previously[39,40] (GAA Custom Engineering, LLC, Kennewick, WA). It should be noted that ions spend ~6 ms transiting the rear ion funnel and contributing both a time delay and a small amount of mobility-based separation to the Arrival Time Distributions (ATD). As the system was designed and optimized for peptide mixture analyses, the rear ion funnel has a low m/z cutoff of ~380. This prevents ions below m/z ~ 380 that can be transmitted through the SLIM, or accumulated and trapped extended periods in the SLIM, from being detected. Thus, even though we did not inject ions below ~ m/z 350 into the SLIM (the estimated m/z cutoff of the front ion funnel), ions of m/z ~ 200 to 380 that are *formed in the SLIM,* such as by dissociation, will not be detected. This effective detection "blind spot" is evident (or likely) in several of the experimental results, as we note in each case. All experiments were performed in triplicate to assess the reproducibility of the result, and each replicate was a sum of nine individual measurements. We note that the three peptides used in this study were selected as a balance between a single

https://doi.org/10.1021/jasms.3c00389
J. Am. Soc. Mass Spectrom. 2024, 35, 365−377

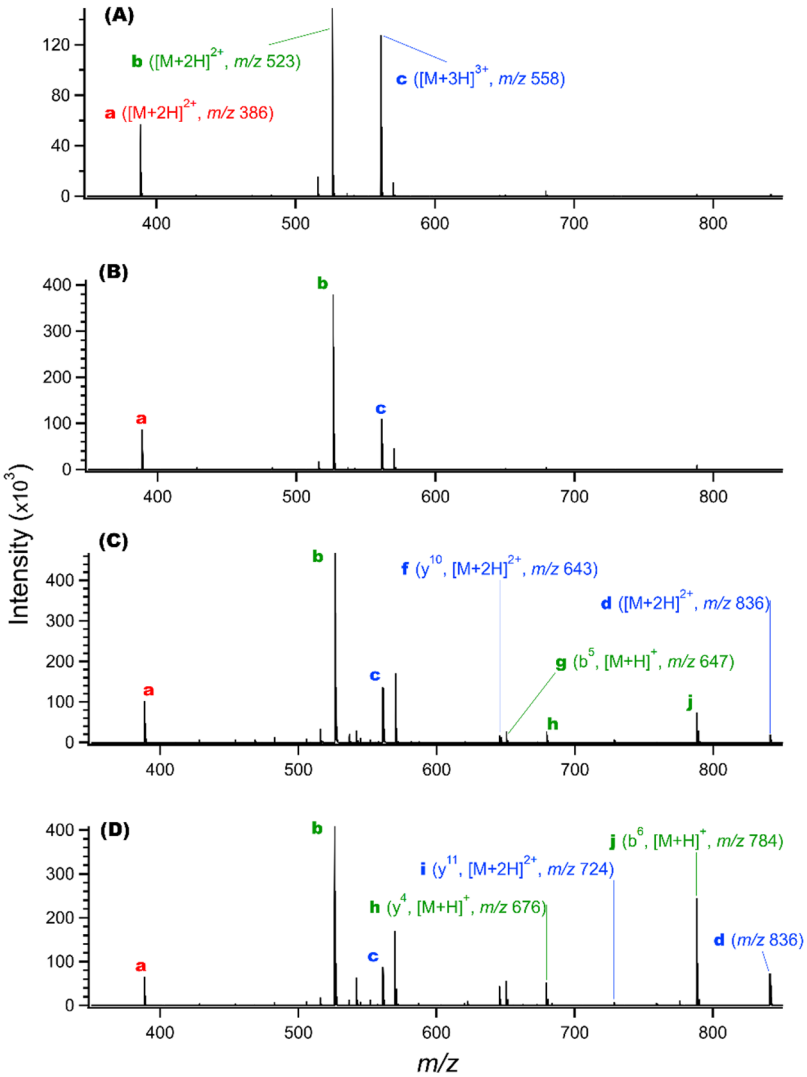

Figure 3. Mass spectra integrated over the range of arrival times for the data shown in Figure 2 for accumulation times of (A) 49, (B) 163 s, (C) 326, and (D) 652 ms using an 8 $V_{p\text{-}p}$ TW amplitude. The three peptide precursor ions (Kemptide (2+), Angiotensin II (2+), and Neurotensin (3+) at m/z 386, 523, and 558 (peaks a, b, and c) are indicated in A, where they dominate the spectrum. (A) 49 and (B) 163 s accumulation times provided efficient ion utilization and conventional spectra, while longer accumulation times result in decreased relative abundances of the three peptide precursor ions and the appearance of additional ion species resulting from their charge loss or fragmentation (e.g., peaks (d)−(j); see text for additional description). The product fragment ion labels are color coded to match their precursor ions.

compound and a complex mixture and to be sensitive to dissociation so as to provide additional insights into potential ion activation during accumulation.

SLIM Module Design. The SLIM module developed for this work was fabricated of FR4 material (woven glass with epoxy) and used TW, RF, and guard electrode dimensions similar to those described previously.[36] The 45.8 cm path of the SLIM module (Figure 1) has three distinct regions (A, B, and C) that used independently controlled TW. The short ion introduction region A (0.9 cm long) used a 5 $V_{p\text{-}p}$ TW amplitude that simply served to transfer ions to the accumulation region B (30.7 cm long) that used TW of different amplitudes (8, 15, and 20 $V_{p\text{-}p}$). This region is followed by region C (14.2 cm long), which used a TW amplitude of 30 $V_{p\text{-}p}$, sufficient to cause ion "surfing", to maintain the temporal profiles of ion populations exiting region B. The TW speed in all three regions was 160 m/s (i.e., only the TW amplitude of region B was varied in this work).

At the end of region B two rows of nominally TW electrodes (Figure 1, red) with 50 and 80 V applied, respectively, were used for a portion of the time as an ion "gate" to prevent the passage of ions; the voltage applied to these electrodes could be changed between either a fixed DC voltage (i.e., the gate's blocking voltage) or set to the appropriate TW potentials (for "opening the gate"). This determined whether ions were trapped in region B or transmitted into region C, where they would surf to the SLIM exit (and then be transmitted through the rear ion funnel to the mass spectrometer, with the exception of ions lost due to its low m/z cutoff, as noted above). For the ATD, as shown in Figure 2, the gate blocking voltage was held constant for an additional 8 ms after the completion of ion accumulation.

RESULTS AND DISCUSSION

We explored the use of much larger ion populations than typical with IMS by using greatly extended ion accumulation periods. Possible space charge effects in this work can arise due

https://doi.org/10.1021/jasms.3c00389
J. Am. Soc. Mass Spectrom. 2024, 35, 365−377

to the size of the ion populations but also the high charge densities achieved in the extended SLIM ion volume due to the opposing fields of the TW and the ion gate (blocking voltage). We emphasize that the TW conditions used in this work would not result in space charge effects for conventional ion accumulation times and population sizes. For TWIMS the TW amplitude is generally chosen to optimize separations and their R_p. Here the TW amplitudes used during ion accumulation are much smaller than those typically used for separations, causing ions to move relatively slowly through the linear SLIM track while being confined in orthogonal directions. Once ions are accumulated in region B (Figure 1) in some experiments they were also stored for additional time before removal of the gate blocking voltage. Removal of the gate potential allows ions to enter region C where they "surf" at the speed of the TW (due to its higher amplitude of 30 V_{p-p}) to the exit of the SLIM and are transferred to the MS. As noted in the Experimental Section, a small amount of mobility separation can occur post-SLIM, primarily in the rear ion funnel; however, this contribution is generally small and insignificant (see later discussion). Thus, the arrival time distributions (ATD), such as shown in Figure 2, closely mirror the ion distributions in departing region B, providing a basis for exploring the evolution of ion populations during accumulation and the effects of space charge.

Peptide Precursor and Total Ion Signal Spatial Distributions Resulting from Extended Ion Accumulation Events. Figure 2 shows the ATD at the MS detector (after gate removal) using the lowest TW amplitude (8 V_{p-p}) in region B for ion accumulation times of 49, 163, 326, and 652 ms. Profiles are shown for the three major peptide precursor ions, where the red, green, and blue traces represent the multiply protonated (e.g., $[M+xH]^{x+}$) Kemptide (2+), Angiotensin II (2+), and Neurotensin (3+) precursors, respectively, and the black traces show the total ion signal (TIS). Figure 3 shows mass spectra for the four accumulation times shown in Figure 2.

The ~9 ms period delay (after opening the gate) before the detection of ions evident in Figure 2 is due to the combined contributions of the time ions spend traversing region C (~1 ms), the rear ion funnel in a field of 9.8 V/cm (~6 ms), and the lower pressure regions to the TOF MS (~1.5 ms). No significant mobility separation can occur in the first and last of these, as the ions surf in region C and the pressure is insufficient after the rear ion funnel. However, a small extent of mobility separation *can* occur while transiting the rear ion funnel and that can be estimated based upon the known CCS for the ions or DTIMS measurements (see Supporting Information; Figure S1). This small contribution will be most significant between Kemptide (2+) and Neurotensin (3+) (~0.5 ms difference), and even smaller (~0.4 to <0.05 ms difference, depending upon the conformers present) between Neurotensin (3+) and Angiotensin II (2+).

The precursor ion ATD shown in Figure 2A is much different than those in Figure 2B–D. It is evident that this shortest ion accumulation time (49 ms, and the additional 8 ms after the ion injection event ends; 57 ms total) is insufficient for *any* ions to reach the end of region B before the gate was removed. The widths of the peptide ion ATD shown in Figure 2A (~60 ms) are consistent with the ion injection period (49 ms) with some additional broadening due to ion diffusion, mobility differences, and charge–charge repulsive interactions while transiting regions A and B driven by the low 8 V_{p-p} amplitude TW. The relative peak intensities in the mass spectrum for this shortest accumulation time (Figure 3A) show the ion population is largely (>90%) due to the three peptide precursor ions, with a few minor peaks due to background and contaminant ions, and with no significant contributions due to fragmentation of the peptides. Similarly, the TIS area shown in Figure 2A is only slightly larger than the sum of the areas for the three peptide precursor ions.

While not shown here but consistent with previous work,[40] for the shorter accumulation times (including those of Figure 2A,B) we observed the detected relative ion population sizes (i.e., integrated peak areas) to increase approximately linearly with accumulation time. The appearance of the peaks at ~10 to 20 ms for the three peptide precursor ions in Figure 2B–D is attributed to ions increasingly accumulating adjacent to the blocking voltage of the SLIM gate; i.e., as the TW moves an increasing portion of the ions to near the gate's potential barrier. These three longer accumulation times display somewhat distinctive characteristics.

For the 163 ms accumulation time (Figure 2B) the total ion population, judged by the integrated TIS, has increased in proportion with accumulation time, and the integrated TIS is only slightly larger than the summed contributions of the peptide precursor ions, as evident in Figure 2A. Additionally, no significant ion dissociation is evident in Figure 3B even though a large fraction of the ions have sufficient time to collect near the gate (see later discussion). We emphasize that the data shown in Figures 2A,B and 3A,B using an 8 V_{p-p} amplitude TW and ion accumulation times of up to 163 ms indicate that ion accumulation in such cases is both efficient (i.e., avoids ion losses) and does not cause significant ion heating.

The TIS continues to increase approximately linearly for the next longest accumulation time (326 ms; Figure 2C); the TIS is approximately double that of Figure 2B (which used a 163 ms accumulation time). However, the TIS maximum intensity is more than twice as large, an observation attributed to the additional time allowing a more compact (i.e., greater ion density) distribution to form near the gate. This maximum TIS (~360 × 10^3 on the consistent arbitrary scale used for the measurements in this work) is close to the maximum observed in these studies. This peak maximum TIS is not exceeded regardless of ion accumulation time, and we assume it approximately corresponds to the maximum ion density that is feasible due to space charge limitations for the ions studied. Similarly, we note that the individual peptide precursor peaks are somewhat narrower in width, consistent with the somewhat increased fraction of ions accumulated near the gate. Interestingly, the corresponding mass spectrum (Figure 3C) shows small but significant new contributions due to ions from the reaction or dissociation of the peptide precursor ions. [It should be noted that no dissociation products are observed below ~ m/z 380 even though several fragment ions should be formed, e.g., by dissociation of Kemptide (2+), and attributed to the low m/z cutoff of the rear ion funnel for ions exiting the SLIM (see Experimental Section).]

For the longest accumulation time (652 ms), all three peptide precursor ions show significantly decreased populations based upon their peak areas, and the mass spectrum (Figure 3D) is now dominated by reaction and fragmentation products. Also of note is the relatively increased TIS at longer arrival times (see discussion below related to space charge induced ion heating). [We note also a decreased maximum in

https://doi.org/10.1021/jasms.3c00389
J. Am. Soc. Mass Spectrom. 2024, 35, 365–377

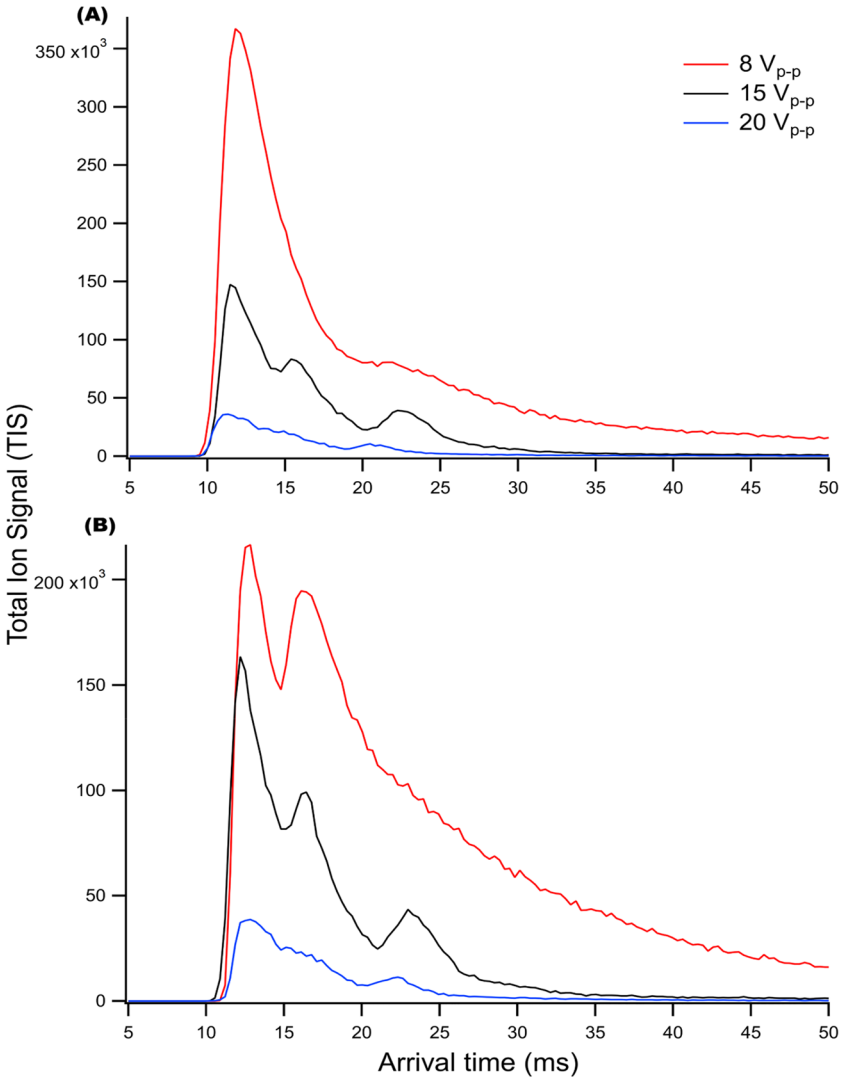

Figure 4. ATD for ions accumulated in region B from the ESI of the peptide mixture. TIS is shown for accumulation times of (A) 326 and (B) 652 ms using TW amplitudes of 8, 15, and 20 $V_{p\text{-}p}$. The smaller ion population sizes evident for larger TW amplitudes is a combined result of ion losses and undetected lower m/z species (see Experimental Section).

the TIS (to ~220 × 10^3). Rather than an actual decrease in the ion density near the gate for this longest accumulation time, we attribute this to "unobserved" lower m/z (<380) species formed by fragmentation of ions close to the gate (see later discussion) that are not transmitted through the rear ion funnel, and thus not detected.]

The ATD in Figure 2B–D show most ions have time to reach the gate region and form profiles with distinct peaks, but also have ~100 ms "tails" attributed to ions that have insufficient time to reach the area near the gate. The tail lengths are limited by the combined length of regions A and B and their lengths correspond to the time required for these ions to migrate to the gate; thus ~100 ms. This estimate is also consistent with the failure of ions to reach the gate for the 49 ms ion accumulation period (Figure 2A). Based upon these observations and the path length (31.8 cm), we can see that ions have average translational speeds of only ~3 m/s in the low amplitude 8 $V_{p\text{-}p}$ 160 m/s TW.

Peptide Precursor Peak ATD Differences for Ions Accumulated near the Gate. A subtle observation from Figure 2B–D is the small but significant differences in both the peak apex arrival times as well as the peak widths for the three peptide precursor ion species; i.e., some separation occurs. This observation applies for both longer accumulation times and extended storage times (as discussed below). The data shown for the peptide precursor ions in Figure 2 were acquired under conditions where only minor mobility-based separations can occur post-SLIM, as discussed above. However, the observed distributions may also be partly attributed to a small extent of separation as ions move through region B and before their arrival at the gate region (see Figure 2A). As we discuss below, this work supports a third (space charge-related) contribution, and that is manifested in much more dramatic fashion for other ions.

As ions accumulate at the gate (Figure 2B–D) Kemptide (2+), which has the highest mobility of the three peptide precursor ions, forms the peak closest to the gate. The proximity to the gate for Kemptide (2+) persists with longer accumulation times. The peaks for the three precursor ions also narrow somewhat with increased accumulation time, most evident for Angiotensin II (2+) between Figure 2B and D.

Thus, the three precursor species have somewhat different proximities to the gate on average. (Since the "readout" after the gate is opened inevitably results in some degree of mixing

https://doi.org/10.1021/jasms.3c00389
J. Am. Soc. Mass Spectrom. 2024, 35, 365−377

during the period between gate removal and ions entering region C, the actual separations for these species may be significantly better than indicated by Figure 2, as we discuss later.) Importantly, we note that the three peptide precursor distributions are arranged according to their mobilities, with the first (closest to the gate; shortest arrival time) and narrowest being for the higher mobility Kemptide (2+), and the last being for the lower mobility Angiotensin II (2+). We also note that the relative size of the three precursor ion populations changes, with decreased relative abundance most evident for the higher mobility Kemptide (2+) for longer accumulation times. These observations are also reflected in the mass spectra shown in Figure 3.

The data indicate that the rates of dissociation and ion−molecule reactions for the precursor ions, such as proton transfer to gas phase impurities, are considerably greater for ions closest to the gate for the longer accumulation times and where the highest ion densities are achieved. These observations are discussed in detail below related to the separations observed for these additional dissociation and ion−molecule reaction product ion species.

The Effect of an Additional Storage Time on Accumulated Ion Populations. Based upon the behavior observed using extended ion accumulation events, we also explored the effect of additional storage times on the accumulated ion populations. As an example, Figure S2 (Supporting Information) shows the effects of adding storage times of up to 163 ms following ion accumulation. Figure S2A shows the same data given in Figure 2C, while Figure S2B−D shows changes with the added storage times that are consistent with the observations and discussion.

In general, we observe that changes due to extended storage time are less dramatic than for extended accumulation times and that the ion populations can be maintained without significant losses *except for the highest mobility species*, as most evident for Kemptide (2+); see Figure S2D. Also observed is some modest narrowing of the peaks and reduction of their integrated TIS intensities with increased storage time, with ion losses being much more prominent for the higher mobility ions ($Kemptide^{2+}$) than the lower mobility ions ($Angiotensin^{2+}$). As discussed in detail later, extended storage times also led to increasing charge reduction of the Neurotensin (3+) ions to the lower charge state (2+) (Figure S3).

We note that the gradual loss of the peak tails as the additional storage time allows more ions to approach the gate. However, even for the longest storage time (Figure S2D) the TIS profile extends to > ∼60 ms. Clearly the relatively intense tails evident for the longest storage times are not simply due to insufficient time for ions to reach the gate region. Indeed, these data suggest that these TIS profile "shapes" are primarily dictated by the ion population size and the combined ion accumulation and added storage time, in addition to the TW amplitude "pushing" ions toward the gate.

Variation in the Total Ion Populations with Extended Accumulation Times Using Increased TW Amplitudes. For most practical applications, the effects due to excessive space charge, such as ion heating, are undesired, and appropriate ion accumulation conditions would include those corresponding to Figure 2A or B. In cases such as shown in Figure 2B significant gains in S/N and IMS R_p compared to Figure 2A would also be expected after accumulation due to the greater peak intensity and decreased peak width for accumulated ions. Even longer accumulation times, as shown in Figure 2C, can be attractive for some applications due to the greater peptide precursor ion peak intensities and decreased peak widths evident when some extent of ion heating is not problematic. However, longer accumulation times (e.g., 652 ms; Figure 2D) suffer from both increased fragmentation and decreased peptide precursor ion peak intensities, and the overall efficiency of ion accumulation falls significantly. Most approaches and applications benefit from avoiding such accumulation conditions for the present SLIM design.

The ion population densities near the gate evident in Figure 2B−D result from the use of a relatively weak 8 $V_{p\text{-}p}$ TW in region B. The trend observed with increased accumulation times is further amplified by the use of higher TW amplitudes that substantially speeds the buildup of ions near the gate. Figure 4 shows the TIS for 326 and 652 ms accumulation times for TW amplitudes of 8, 15, and 20 $V_{p\text{-}p}$. As noted earlier, longer accumulation times using an 8 $V_{p\text{-}p}$ TW amplitude led to a reduced overall efficiency of ion accumulation. The greater TW amplitudes resulted in further significant decreases in the overall efficiency of ion accumulation. The large decreases evident in the TIS amplitude may be at least partly attributed to greater dissociation of the peptides to form fragments that are precluded from detection due to the 380 m/z cutoff of the rear ion funnel (see discussion below) and species of lower mobility that are precluded from detection. Consistent also with this is the subtle shift to longer arrival times for the TIS onset with both increased accumulation time and greater TW amplitude, which we can also attribute to increased abundances for lower m/z (and higher mobility) fragments also precluded from detection, as discussed earlier.

It is expected that space charge limited ion densities should be rapidly achieved near the gate with the use of higher TW amplitudes, but in fact the large decreases are observed for the maximum TIS. This is likely due to a combination of factors, such as the space charge limited ion density region being made up of lower m/z species that can be trapped in the SLIM but not detected (due to loss to the low m/z cutoff of the rear ion funnel) or this region being too small to be reflected by the measurements (due to an effective averaging over some range of arrival times). Clearly, additional studies, both computational (simulations) and experimental, will be necessary to better understand these observations. However, it is also clear that one should avoid the use of higher amplitude TWs in conjunction with greatly extended accumulation times or ion populations; i.e., where space charge limited ion densities are achieved.

In the remainder of this work, we utilize the relatively gentle 8 $V_{p\text{-}p}$ TW due to its much greater relevance for practical applications.

Ion Population Changes with Increased (or "Excessive") Ion Population Densities. For RF-based ion confinement (e.g., using a stacked ring ion guide, multipole ion trap, ion funnel, etc.), there is generally a volume where the likelihood of ion heating due to the RF fields will be negligible and where ions will ideally (for most purposes) reside. Ion excursions into areas where they experience greater RF fields will increase ion translational energies and lead to internal excitation upon collisions, potentially increasing ion losses and fragmentation.

As the overall ion population increases and more ions accumulate near the gate, a peak is formed in the TIS arrival time profile. As the peaks' ion density increases, at some point it is reasonable to expect that the maximum feasible ion density

https://doi.org/10.1021/jasms.3c00389
J. Am. Soc. Mass Spectrom. 2024, 35, 365−377

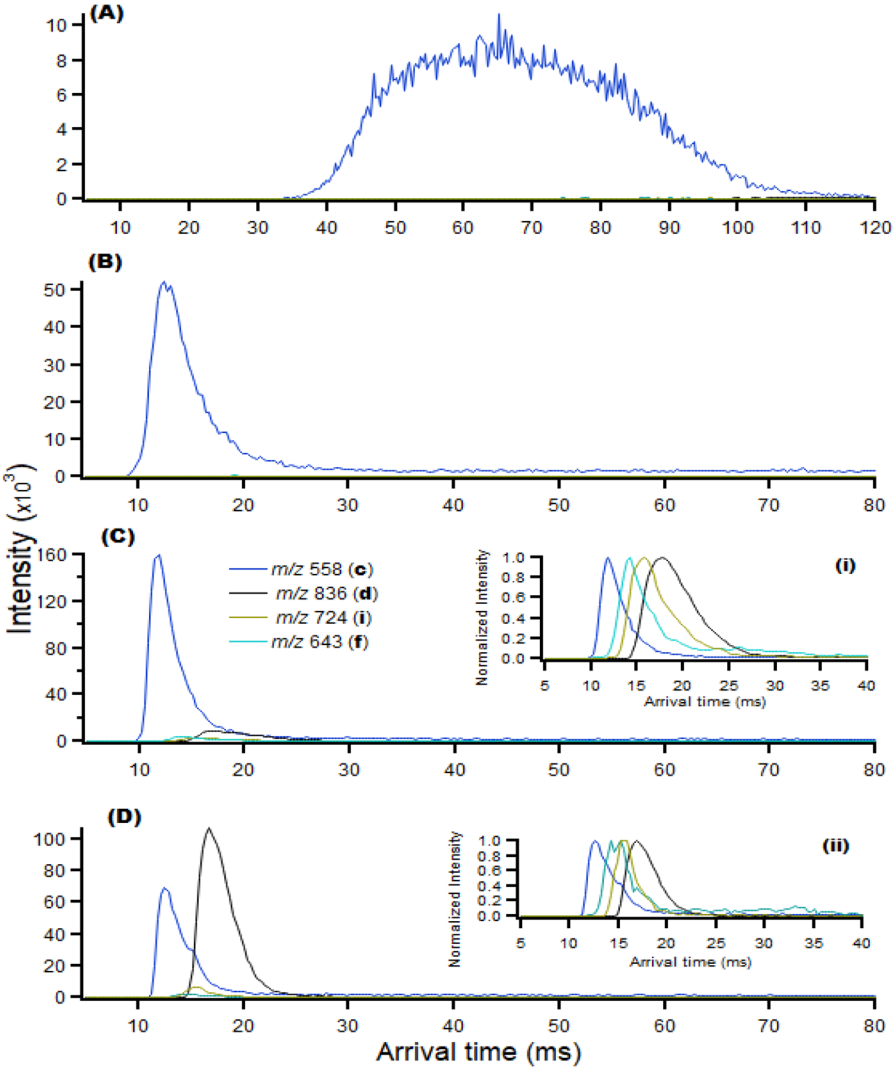

Figure 5. ATD on an absolute scale and a normalized scale (insets i and ii to C and D) for Neurotensin (3+) and (2+), *m/z* 558 and 836, as well as two of its more prominent fragment ions (y,[10] *m/z* 643 and y,[11] *m/z* 724; peaks i and f in Figure 3) for different ion accumulation times. For the two shortest accumulation times, 49 ms (A) and 163 ms (B), where space charge effects are minimized, the Neurotensin (3+) charge state (blue) dominates. For longer accumulation times, 326 ms (C) and 652 ms (D), the Neurotensin (2+) charge state (black) and several fragment ions become increasingly prominent, forming peaks with distinct arrival times.

in this region will be limited due to charge−charge repulsion (i.e., space charge), whereupon the ion cloud will expand spatially in some fashion. This expansion can be "backward" along the TW track (leading to longer arrival times), laterally between the DC guard electrodes, or toward the SLIM surfaces and the RF electrodes. Such spatial expansion can lead to ion activation or loss depending on details of the confining potentials (or RF-generated pseudopotentials) in each dimension. Based upon such reasoning, we anticipate that sufficiently low TW amplitudes in trapping/storage volumes would avoid ion cloud expansion in orthogonal directions that cause ion loss or heating effects. In this regard, we have recently demonstrated effective ion accumulation and extended storage *after selection from IMS separations* using very low TW amplitudes in SLIM trapping regions.[53]

The present data show the ion populations (TIS) shift closer to the gate with increased TW amplitude or time as well as a dramatic effect on the size of the accumulated ion populations.

The present data also indicate that ion heating occurs for the densest region of the ion population close to the gate and when the ion density is space charge-limited in this region. The arrival time distributions in Figure 2 show Kemptide (2+) to be closest to the gate and have the narrowest distribution. Kemptide (2+) also experiences a significant relative population decrease as accumulation time increases (Figure 2B−D). The longest accumulation times show the "next" precursor peptide ion, Neurotensin (3+), to also show a relative population decrease in conjunction with the appearance of distinctive fragment ions. Thus, these data are consistent with a small fraction of the overall ion population that is near to the gate being selectively subject to significant excitation and dissociation, and this region being sufficiently large to encompass portions of both the Kemptide (2+) and Neurotension (3+) populations.

Spatial Variation of Lower Mobility Ions Formed with Extended Accumulation Times: More Definitive Evidence for Space Charge-Driven Separations. As noted earlier, the accumulated peptide precursor ions (the distributions shown in Figure 2A) appear to be "rearranged" to some extent after arrival near the gate. However, while the peptide

https://doi.org/10.1021/jasms.3c00389
J. Am. Soc. Mass Spectrom. 2024, 35, 365−377

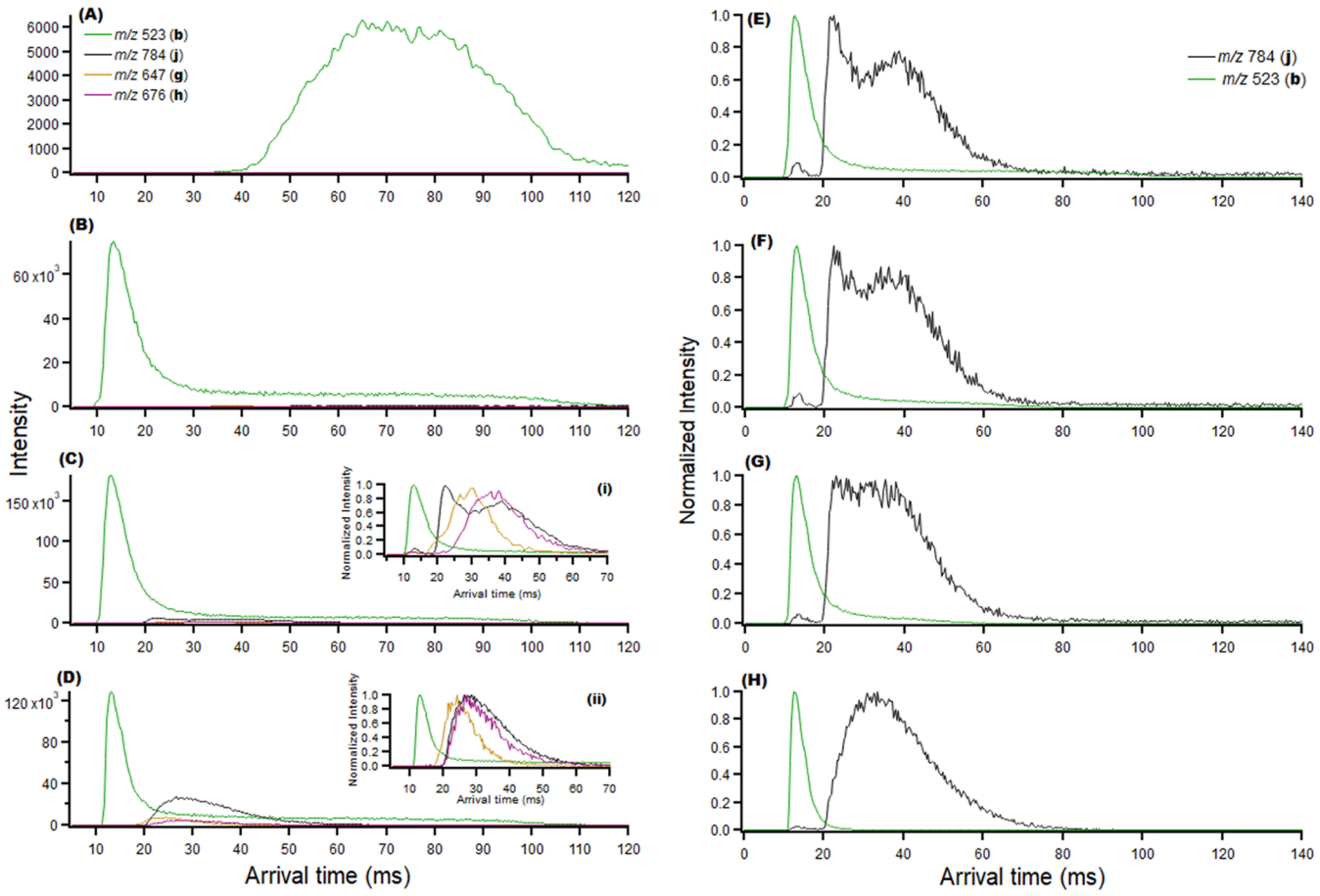

Figure 6. (Left) ATD for accumulation times of (A) 49, (B) 163, (C) 326, and (D) 652 ms for Angiotensin II (2+), m/z 523, a green trace, and three of its fragment ions (b^5 m/z 647, y^4 m/z 676, and b^6 m/z 784). (Right) Normalized ATD for an ion accumulation time of 326 ms and additional storage times of (E) 8, (F) 41, (G) 57, and (H) 163 ms for Angiotensin II (2+) and its m/z 784 b^6 fragment (black trace).

precursor ion distributions show unexpected and striking behavior for the accumulated and stored ion populations, they nevertheless are relatively subtle effects that also are convoluted by some minor separation in the rear ion funnel, as discussed earlier.

Much more striking behavior is observed for other lower mobility ions formed by reactions of the peptide precursor ions, which we now discuss. As already noted, the longer accumulation periods result in increasing contributions due to fragmentation or reactions of the peptide precursor ions. As a prominent example, the mass spectra in Figure 3 show significant contributions of Neurotensin (2+), m/z 836, only for the longer accumulation times. Consistently, we observed increased Neurotensin (2+) for conditions favoring ion activation: with larger ion populations, longer storage times, and higher TW amplitudes. Neurotensin (2+) likely results from proton-transfer reactions by Neurotensin (3+) (e.g., with gas-phase contaminants) at increased rates upon ion activation. We note also that similar proton transfer processes have also recently been observed for larger numbers of ion trapping events (i.e., accumulation of larger ion populations) and in a SLIM array of traps using a similar ion confinement gate arrangement.[53]

Figure 5 shows data for the two charge states of Neurotensin (3+ and 2+; m/z 558 and 836) as well as its two prominent fragments (y_{10} m/z 643 and y_{11} m/z 724; peaks i and f in Figure 3) for different ion accumulation times. The data are also given on normalized scales for the longest accumulation times (Figure 5C,D insets) to better show the differences in peak arrival times. While Neurotensin (2+) ion population is not significant for the shortest accumulation times (Figure 5A,B), it becomes readily observable for the 326 ms accumulation time (Figure 5C), but with only ~10% of the ion population for the 3+ charge state based upon the peak areas. For the longest 652 ms accumulation time (Figure 5D) the 3+ ions have a significantly smaller peak area than for the shorter accumulation time and the 2+ charge state is greater. Clearly, the 2+ charge state ions are formed in the SLIM from the 3+ charge state. This dramatic change in relative abundance for these species is attributed to reactions in a limited region near the gate where the 3+ ions experience significant space charge related excitation. We conclude that Kemptide (2+) has been sufficiently depleted due to ion heating "to make space" for it in the region of highest ion density, and leading to its activation.

Even more striking than these abundance changes are the different ATD for the two Neurotensin charge states; Figure 5 shows their arrival time distribution peaks to be mostly resolved. Not only is resolution for the two species observed, but the Neurotensin (2+) is formed largely from previously accumulated Neurotensin (3+) ions near the gate. Thus, Neurotensin (2+) ions have moved in the *opposite direction of the TW!* Similar trends are evident for the two lower intensity Neurotensin fragment ions shown in Figure 5C,D insets on a

https://doi.org/10.1021/jasms.3c00389
J. Am. Soc. Mass Spectrom. 2024, 35, 365−377

normalized scale, with the two fragments forming peaks between the two Neurotensin charge states. This behavior is also observed with increased storage times after accumulation for both the precursor and fragment ions. Figure S3 shows data for a 326 ms accumulation time, with a range of added storage times, showing both a decrease in the 3+ charge state and an increase in the 2+ charge state with an increased storage time. Again, it appears that upon formation the lower charge state ions move in a direction opposite the TW and contribute to a population much further from the gate than their precursor ions.

Figure 6 shows the changes for Angiotensin II (2+) peak intensities for different accumulation times and that are consistent with the above discussion. Figure 6A−D (left) shows the arrival time distributions on an absolute scale for Angiotensin II (2+) and the three prominent fragment ions (b^5 m/z 647, y^4 m/z 676, and b^6 m/z 784) and on a normalized scale in Figure 6C,D insets for the different accumulation times. Figure 6E−H (right) shows Angiotensin II (2+) and its m/z 784 fragment on normalized scales for the 326 ms ion accumulation time and additional storage times. Consistent with the data for Neurotensin ions, Figure 6A−D (left) shows a decrease for the precursor ion population accompanied by an increase in fragment ion populations at longer arrival times. Small contributions can also be seen for the reaction products at the location of the precursor ion near the gate (most evident for the 326 ms accumulation time; see inset to Figure 6 C), i.e., before moving to the peak at longer arrival times.

Figure 6E−H shows Angiotensin II (2+) and the b_6^+ fragment (m/z 784) with increasing storage times after the 326 ms accumulation event and where the fragment ion intensity increases significantly during storage. This fragment initially displays a complex profile (see Figure 6E) immediately following the end of accumulation and with a smaller but significant component at the same arrival time as Angiotensin II (2+). Thus, this portion of the fragment ion population apparently arises from Angiotensin II (2+) dissociation near the gate. Consistent with this observation is that the relative magnitude of Angiotensin II (2+) decreases as the later arrival time (m/z 784) distribution increases with increased storage time. This second broad distribution (at ∼25 to 60 ms) is centered at ∼35 ms. The origin of the complex distribution is uncertain, but the component at ∼25 ms appears correlated with the intensity of the short arrival time peak, suggesting it is related to ions "in transit" between the distributions. In should be noted that we observe at least two conformers for Angiotensin II (2+) using DTIMS (see Supporting Information Figure S1) and Clemmer and co-workers[54] have previously observed multiple conformers for both the precursor and fragment ions for Angiotensin II (2+), and the broad fragment ion distribution we observe may include such conformers.

These data are again consistent with the activation of ions in a limited volume close to the gate as well as the migration of lower mobility ions formed in this volume against the direction of the TW to form stable peaks detected at later arrival times.

The Implications of Space Charge-Driven Ion Separations. Based upon the above discussion, we conclude that ions are rearranging and focusing to form peaks along the SLIM track volume due to the opposing forces arising from space charge and the TW. The data indicate that the arrival time for a particular species after accumulation and storage (and any subsequent stacking or focusing) depends on the other species present, as long as the ion population is "continuous", i.e., has no significant gaps in the charge distribution along the track axis. That is, we expect trapped ion population density to decrease in a distinctive fashion from its maxima near the gate due to the opposing forces of the self-generated space charge and the TWs. The Figure 4 ATD shows that the initial decrease in ion population density along the track axis is steep, and thus better separations might be expected due to differences in space charge that are manifested at shorter arrival times. Similarly, better separations might be anticipated for lower temperature ion populations, and perhaps using more gentle uniform drift fields rather than low amplitude traveling waves.

Importantly, the use of a lower TW amplitude while accumulating ions is expected to effectively build a population that spreads further from the gate for a given total number of charges and result in broader peaks in the ATD. More ions (e.g., from longer accumulation times) and lower TW amplitudes are thus expected to allow ions to use more of the available volume. Attractive is the use of a TW amplitude that is sufficiently low to enable accumulation of large ion populations with minimal ion heating. To some extent, the "length" (i.e., the peak or ion population distribution width) can be controlled in a useful fashion by simply adjusting the accumulation/storage time. Since longer trapping times increase the maximum ion density, a more rapid accumulation of a given population should also result in less ion heating.

We believe the present space charge induced separation findings are novel and note that the conditions under which we observe these phenomena can potentially apply for measurements in other more conventional instrumentation where large trapping volumes and high ion population densities are achieved. This can include linear ion traps, stacked ring ion guides, and ion funnels that are operated in ways generally avoided (e.g., locating a stopping potential at the bottom of an ion funnel having a gentle field gradient). One potentially related observation is by Causon et al.,[55] who conducted simulations on the effects of significant space charge on ion transmission through an IFT. They observed 'space charge from the first ions to accumulate causes later arriving ions to shift further back and toward the [IFT] rings' and 'low m/z ions are lost ahead of higher m/z ions as space charge builds up'. This was viewed as consistent with the loss of very low m/z ions observed in measurements. Based upon their simulations, they also suggest that the highest mobility ions in the IFT more readily expand into the pseudopotential created by the RF, an observation consistent with the preferential heating observed for such species in the gate vicinity in this work. While clearly different from the present SLIM arrangement, their simulations are consistent with space charge playing a role in the observed mobility-based spatial distributions.

It must be noted that we are for the present implicitly ignoring possible spatial variation for accumulated and stored ions in orthogonal directions (i.e., toward the SLIM surfaces or the side). Previous work for RF multipoles and stacked ring ion guides has indicated some significant spatial variations in ion densities,[56] as well as m/z-based stratification (i.e., separation),[57] can occur, and comparable phenomena may occur here. While this needs to be considered in future computational studies, at present, we assume that any such spatial variation does not significantly impact ion population changes at the center of distribution along the SLIM track axis.

https://doi.org/10.1021/jasms.3c00389
J. Am. Soc. Mass Spectrom. 2024, 35, 365−377

The Potential Utility of Space Charge-Driven Ion Separations. While these phenomena need additional experimental and computational study from a fundamental perspective, ion separations under conditions of significant space charge in trapped ion volumes are potentially of significant practical utility. The observed phenomena suggest potentially significant value for ion manipulations, such as ion prefractionation before MS and IMS-MS, for purposes that include improving the sensitivity or dynamic range of analyses. For IMS separations, the narrowing of the starting distribution for one or more constituents in a given volume allows larger ion populations to be used without degrading the resolving power. These separations can potentially be significantly optimized by use of larger ion volumes, such as in extended SLIM track lengths, as well as the use of "cooler" ion populations, optimized fields, etc. One potential type of application that can be envisioned would use two "bracketing" species to enrich a targeted species (having a specific mobility between the two) to improve the sensitivity of measurements.

While the present separations are driven by space charge, they do not necessarily cause ion heating, which appears to occur only in the region of the highest ion density. Both increased ion populations near the gate and longer storage times led to increased ion heating and fragmentation in this region. The observed separations result in ion heating being limited to the highest mobility species that populate the region of the highest ion density. Importantly, this work suggests that conditions that cause ion heating should be avoidable, e.g., by the use of a sufficiently small TW amplitude or limiting accumulation times while retaining significant benefits from space charge-driven ion separations.

CONCLUSIONS

The trapping and accumulation of ions as a prelude to IMS separations is important for sensitive measurements and the resolving power achievable, and key aspects involve both the size of the ion population and their spatial distribution. We have studied the accumulation and storage of ions using traveling waves in a SLIM region having an extended linear path and evaluated the effects of ion population size and storage time. This charge density of the trapped ion cloud is ultimately limited by space charge, and when this limit is reached, ions can experience increased ion heating (i.e., activation) that can be manifested also as ion losses and/or dissociation. We find that lower TW amplitudes that provide a gentler "push" toward a confinement potential can have significant utility for decreasing the width of the accumulated ion packet and thus improving resolving power. Ideally, the TW amplitude is sufficiently low that the opposing forces due to space charge can prevent an excessively large ion density, so that the ion cloud expansion is in the direction opposite the TWs, ultimately providing a distribution width that is minimized for a given ion population.

For IMS applications this work shows that the accumulation process can be optimized to prevent significant distribution width contributions from degrading resolving power or causing significant peak "tails" that could distort peak shapes after separation. It also suggests the use of an "in-SLIM" ion accumulation region length no longer than needed to achieve a desired peak width and located close to the SLIM entrance as advantageous for speeding accumulation, enhancing overall ion utilization efficiency and avoiding ion population profiles that can result in peak tailing.

A novel observation from this work is that ions separate to some extent in the SLIM track accumulation volume by their mobilities due to the opposing forces arising from space charge and the TW. An important implication of these separations is that the space charge induced ion heating is restricted to the highest mobility ions that populate the highest ion population density region close to the ion gate.

This work also indicates that the spatial distribution for a particular species during accumulation and storage (and any subsequent ion "stacking" or "focusing") depends on the other species present. The detected ion population density drops in a distinctive fashion with the distance from the gate. Ions locate or stack with decreasing mobility with distance from the gate. Fragment ions formed by ion heating at the gate that have lower mobility than their precursor ion (e.g., a lower charge state formed by proton transfer) will move counter to the TW, forming a peak at a greater distance from the gate. Such separations have potential utility for cases where the use of extremely large ion populations is attractive, such as for ion fractionation to provide a greater dynamic range to overall measurements, or the collection of materials by surface deposition (or "soft-landing").

In this study, we have used traveling waves to drive ions toward the gate for ion accumulation, creating the space charge conditions causing mobility based separations. It is likely that the observed phenomena and similar (and potentially better) separations would result from the use of a constant drift field, and this will be the subject of a future study.

ASSOCIATED CONTENT

Supporting Information

The Supporting Information is available free of charge at https://pubs.acs.org/doi/10.1021/jasms.3c00389.

> Additional results include drift tube IMS arrival time distribution for the three peptide precursor ions; arrival time distributions of the three peptide precursor ions and TIS using ion accumulation time of 326 ms and different storage times; arrival time distributions on absolute and normalized scales for Neurotensin (3+) and (2+) using an ion accumulation time of 326 ms and different storage times (PDF)

AUTHOR INFORMATION

Corresponding Author

Richard D. Smith − *Biological Sciences Division, Pacific Northwest National Laboratory, Richland, Washington 99354, United States;* orcid.org/0000-0002-2381-2349; Email: rds@pnnl.gov

Authors

Pearl Kwantwi-Barima − *Biological Sciences Division, Pacific Northwest National Laboratory, Richland, Washington 99354, United States*

Sandilya V. B. Garimella − *Biological Sciences Division, Pacific Northwest National Laboratory, Richland, Washington 99354, United States;* orcid.org/0000-0001-6649-9842

Isaac K. Attah − *Biological Sciences Division, Pacific Northwest National Laboratory, Richland, Washington 99354, United States;* orcid.org/0000-0002-9626-2069

https://doi.org/10.1021/jasms.3c00389
J. Am. Soc. Mass Spectrom. 2024, 35, 365−377

Xueyun Zheng − *Biological Sciences Division, Pacific Northwest National Laboratory, Richland, Washington 99354, United States;* orcid.org/0000-0001-9782-4521
Yehia M. Ibrahim − *Biological Sciences Division, Pacific Northwest National Laboratory, Richland, Washington 99354, United States;* orcid.org/0000-0001-6085-193X

Complete contact information is available at: https://pubs.acs.org/10.1021/jasms.3c00389

Notes

The authors declare no competing financial interest.

■ ACKNOWLEDGMENTS

The work was supported by the National Institute of General Medical Sciences (grant P41 GM103493-15), and utilized capabilities developed under NIH National Institute of General Medical Sciences (grant R01 GM130709-01). This project was performed in the Environmental Molecular Sciences Laboratory, a DOE OBER national scientific user facility on the Pacific Northwest National Laboratory (PNNL) campus. PNNL is a multiprogram national laboratory operated by Battelle for the DOE under contract DE-AC05-76RL01830.

■ REFERENCES

(1) Gabelica, V.; Marklund, E. Fundamentals of ion mobility spectrometry. *Curr. Opin. Chem. Biol.* **2018**, *42*, 51−59.
(2) Cumeras, R.; Figueras, E.; Davis, C. E.; Baumbach, J. I.; Gràcia, I. Review on Ion Mobility Spectrometry. *Part 1: current instrumentation. Analyst* **2015**, *140* (5), 1376−1390.
(3) Zucker, S. M.; Lee, S.; Webber, N.; Valentine, S. J.; Reilly, J. P.; Clemmer, D. E. An Ion Mobility/Ion Trap/Photodissociation Instrument for Characterization of Ion Structure. *J. Am. Soc. Mass Spectrom.* **2011**, *22* (9), 1477.
(4) Wu, C.; Siems, W. F.; Klasmeier, J.; Hill, H. H. Separation of Isomeric Peptides Using Electrospray Ionization/High-Resolution Ion Mobility Spectrometry. *Anal. Chem.* **2000**, *72* (2), 391−395.
(5) Reid Asbury, G.; Klasmeier, J.; Hill, H. H., Jr Analysis of explosives using electrospray ionization/ion mobility spectrometry (ESI/IMS). *Talanta* **2000**, *50* (6), 1291−1298.
(6) Ewing, R. G.; Atkinson, D. A.; Eiceman, G. A.; Ewing, G. J. A critical review of ion mobility spectrometry for the detection of explosives and explosive related compounds. *Talanta* **2001**, *54* (3), 515−529.
(7) Steiner, W. E.; Klopsch, S. J.; English, W. A.; Clowers, B. H.; Hill, H. H. Detection of a Chemical Warfare Agent Simulant in Various Aerosol Matrixes by Ion Mobility Time-of-Flight Mass Spectrometry. *Anal. Chem.* **2005**, *77* (15), 4792−4799.
(8) Mäkinen, M.; Nousiainen, M.; Sillanpää, M. Ion spectrometric detection technologies for ultra-traces of explosives: A review. *Mass Spectrom. Rev.* **2011**, *30* (5), 940−973.
(9) Kwantwi-Barima, P.; Ouyang, H.; Hogan, C. J.; Clowers, B. H. Tuning Mobility Separation Factors of Chemical Warfare Agent Degradation Products via Selective Ion-Neutral Clustering. *Anal. Chem.* **2017**, *89* (22), 12416−12424.
(10) Márquez-Sillero, I.; Aguilera-Herrador, E.; Cárdenas, S.; Valcárcel, M. Ion-mobility spectrometry for environmental analysis. *TrAC Trends in Analytical Chemistry* **2011**, *30* (5), 677−690.
(11) Celma, A.; Sancho, J. V.; Schymanski, E. L.; Fabregat-Safont, D.; Ibáñez, M.; Goshawk, J.; Barknowitz, G.; Hernández, F.; Bijlsma, L. Improving Target and Suspect Screening High-Resolution Mass Spectrometry Workflows in Environmental Analysis by Ion Mobility Separation. *Environ. Sci. Technol.* **2020**, *54* (23), 15120−15131.
(12) Pringle, S. D.; Giles, K.; Wildgoose, J. L.; Williams, J. P.; Slade, S. E.; Thalassinos, K.; Bateman, R. H.; Bowers, M. T.; Scrivens, J. H. An investigation of the mobility separation of some peptide and protein ions using a new hybrid quadrupole/travelling wave IMS/oa-ToF instrument. *Int. J. Mass Spectrom.* **2007**, *261* (1), 1−12.
(13) Shi, L.; Holliday, A. E.; Shi, H.; Zhu, F.; Ewing, M. A.; Russell, D. H.; Clemmer, D. E. Characterizing Intermediates Along the Transition from Polyproline I to Polyproline II Using Ion Mobility Spectrometry-Mass Spectrometry. *J. Am. Chem. Soc.* **2014**, *136* (36), 12702−12711.
(14) Kłoniecki, M.; Jabłonowska, A.; Poznański, J.; Langridge, J.; Hughes, C.; Campuzano, I.; Giles, K.; Dadlez, M. Ion Mobility Separation Coupled with MS Detects Two Structural States of Alzheimer's Disease Aβ1−40 Peptide Oligomers. *J. Mol. Biol.* **2011**, *407* (1), 110−124.
(15) Dear, G. J.; Munoz-Muriedas, J.; Beaumont, C.; Roberts, A.; Kirk, J.; Williams, J. P.; Campuzano, I. Sites of metabolic substitution: investigating metabolite structures utilising ion mobility and molecular modelling. *Rapid Commun. Mass Spectrom.* **2010**, *24* (21), 3157−3162.
(16) Hinz, C.; Liggi, S.; Griffin, J. L. The potential of Ion Mobility Mass Spectrometry for high-throughput and high-resolution lipidomics. *Curr. Opin. Chem. Biol.* **2018**, *42*, 42−50.
(17) Zheng, X.; Smith, R. D.; Baker, E. S. Recent advances in lipid separations and structural elucidation using mass spectrometry combined with ion mobility spectrometry, ion−molecule reactions and fragmentation approaches. *Curr. Opin. Chem. Biol.* **2018**, *42*, 111−118.
(18) Plasencia, M. D.; Isailovic, D.; Merenbloom, S. I.; Mechref, Y.; Clemmer, D. E. Resolving and assigning N-linked glycan structural isomers from ovalbumin by IMS-MS. *J. Am. Soc. Mass Spectrom.* **2008**, *19* (11), 1706−1715.
(19) Chen, Z.; Glover, M. S.; Li, L. Recent advances in ion mobility−mass spectrometry for improved structural characterization of glycans and glycoconjugates. *Curr. Opin. Chem. Biol.* **2018**, *42*, 1−8.
(20) Ruotolo, B. T.; Benesch, J. L. P.; Sandercock, A. M.; Hyung, S.-J.; Robinson, C. V. Ion mobility−mass spectrometry analysis of large protein complexes. *Nat. Protoc.* **2008**, *3* (7), 1139−1152.
(21) Stow, S. M.; Causon, T. J.; Zheng, X.; Kurulugama, R. T.; Mairinger, T.; May, J. C.; Rennie, E. E.; Baker, E. S.; Smith, R. D.; McLean, J. A.; Hann, S.; Fjeldsted, J. C. An Interlaboratory Evaluation of Drift Tube Ion Mobility−Mass Spectrometry Collision Cross Section Measurements. *Anal. Chem.* **2017**, *89* (17), 9048−9055.
(22) Borsdorf, H.; Eiceman, G. A. Ion Mobility Spectrometry: Principles and Applications. *Appl. Spectrosc. Rev.* **2006**, *41* (4), 323−375.
(23) de la Mora, J. F.; Ude, S.; Thomson, B. A. The potential of differential mobility analysis coupled to MS for the study of very large singly and multiply charged proteins and protein complexes in the gas phase. *Biotechnology Journal* **2006**, *1* (9), 988−997.
(24) Tseng, Y.-H.; Pease, L. F. Electrospray differential mobility analysis for nanoscale medicinal and pharmaceutical applications. *Nanomedicine: Nanotechnology, Biology and Medicine* **2014**, *10* (8), 1591−1600.
(25) Guevremont, R. High-field asymmetric waveform ion mobility spectrometry: A new tool for mass spectrometry. *Journal of Chromatography A* **2004**, *1058* (1), 3−19.
(26) Shvartsburg, A. A.; Li, F.; Tang, K.; Smith, R. D. High-Resolution Field Asymmetric Waveform Ion Mobility Spectrometry Using New Planar Geometry Analyzers. *Anal. Chem.* **2006**, *78* (11), 3706−3714.
(27) Michelmann, K.; Silveira, J. A.; Ridgeway, M. E.; Park, M. A. Fundamentals of Trapped Ion Mobility Spectrometry. *J. Am. Soc. Mass Spectrom.* **2015**, *26* (1), 14−24.
(28) Naylor, C. N.; Ridgeway, M. E.; Park, M. A.; Clowers, B. H. Evaluation of Trapped Ion Mobility Spectrometry Source Conditions Using Benzylammonium Thermometer Ions. *J. Am. Soc. Mass Spectrom.* **2020**, *31* (7), 1593−1602.
(29) Shvartsburg, A. A.; Smith, R. D. Fundamentals of Traveling Wave Ion Mobility Spectrometry. *Anal. Chem.* **2008**, *80* (24), 9689−9699.

(30) Giles, K.; Pringle, S. D.; Worthington, K. R.; Little, D.; Wildgoose, J. L.; Bateman, R. H. Applications of a travelling wave-based radio-frequency-only stacked ring ion guide. *Rapid Commun. Mass Spectrom.* **2004**, *18* (20), 2401−2414.
(31) Bohrer, B. C.; Merenbloom, S. I.; Koeniger, S. L.; Hilderbrand, A. E.; Clemmer, D. E. Biomolecule Analysis by Ion Mobility Spectrometry. *Annual Review of Analytical Chemistry* **2008**, *1* (1), 293−327.
(32) Wojcik, R.; Nagy, G.; Attah, I. K.; Webb, I. K.; Garimella, S. V. B.; Weitz, K. K.; Hollerbach, A.; Monroe, M. E.; Ligare, M. R.; Nielson, F. F.; Norheim, R. V.; Renslow, R. S.; Metz, T. O.; Ibrahim, Y. M.; Smith, R. D. SLIM Ultrahigh Resolution Ion Mobility Spectrometry Separations of Isotopologues and Isotopomers Reveal Mobility Shifts due to Mass Distribution Changes. *Anal. Chem.* **2019**, *91* (18), 11952−11962.
(33) Hamid, A. M.; Ibrahim, Y. M.; Garimella, S. V. B.; Webb, I. K.; Deng, L.; Chen, T.-C.; Anderson, G. A.; Prost, S. A.; Norheim, R. V.; Tolmachev, A. V.; Smith, R. D. Characterization of Traveling Wave Ion Mobility Separations in Structures for Lossless Ion Manipulations. *Anal. Chem.* **2015**, *87* (22), 11301−11308.
(34) Deng, L.; Webb, I. K.; Garimella, S. V. B.; Hamid, A. M.; Zheng, X.; Norheim, R. V.; Prost, S. A.; Anderson, G. A.; Sandoval, J. A.; Baker, E. S.; Ibrahim, Y. M.; Smith, R. D. Serpentine Ultralong Path with Extended Routing (SUPER) High Resolution Traveling Wave Ion Mobility-MS using Structures for Lossless Ion Manipulations. *Anal. Chem.* **2017**, *89* (8), 4628−4634.
(35) Garimella, S. V. B.; Ibrahim, Y. M.; Webb, I. K.; Ipsen, A. B.; Chen, T.-C.; Tolmachev, A. V.; Baker, E. S.; Anderson, G. A.; Smith, R. D. Ion manipulations in structures for lossless ion manipulations (SLIM): computational evaluation of a 90° turn and a switch. *Analyst* **2015**, *140* (20), 6845−6852.
(36) Deng, L.; Ibrahim, Y. M.; Hamid, A. M.; Garimella, S. V. B.; Webb, I. K.; Zheng, X.; Prost, S. A.; Sandoval, J. A.; Norheim, R. V.; Anderson, G. A.; Tolmachev, A. V.; Baker, E. S.; Smith, R. D. Ultra-High Resolution Ion Mobility Separations Utilizing Traveling Waves in a 13 m Serpentine Path Length Structures for Lossless Ion Manipulations Module. *Anal. Chem.* **2016**, *88* (18), 8957−8964.
(37) Knorr, F. J.; Eatherton, R. L.; Siems, W. F.; Hill, H. H. Fourier Transform Ion Mobility Spectrometry. *Anal. Chem.* **1985**, *57* (2), 402−406.
(38) Zheng, X.; Dupuis, K. T.; Aly, N. A.; Zhou, Y.; Smith, F. B.; Tang, K.; Smith, R. D.; Baker, E. S. Utilizing ion mobility spectrometry and mass spectrometry for the analysis of polycyclic aromatic hydrocarbons, polychlorinated biphenyls, polybrominated diphenyl ethers and their metabolites. *Anal. Chim. Acta* **2018**, *1037*, 265−273.
(39) Deng, L.; Ibrahim, Y. M.; Garimella, S. V. B.; Webb, I. K.; Hamid, A. M.; Norheim, R. V.; Prost, S. A.; Sandoval, J. A.; Baker, E. S.; Smith, R. D. Greatly Increasing Trapped Ion Populations for Mobility Separations Using Traveling Waves in Structures for Lossless Ion Manipulations. *Anal. Chem.* **2016**, *88* (20), 10143−10150.
(40) Li, A.; Nagy, G.; Conant, C. R.; Norheim, R. V.; Lee, J. Y.; Giberson, C.; Hollerbach, A. L.; Prabhakaran, V.; Attah, I. K.; Chouinard, C. D.; Prabhakaran, A.; Smith, R. D.; Ibrahim, Y. M.; Garimella, S. V. B. Ion Mobility Spectrometry with High Ion Utilization Efficiency Using Traveling Wave-Based Structures for Lossless Ion Manipulations. *Anal. Chem.* **2020**, *92* (22), 14930−14938.
(41) Clowers, B. H.; Ibrahim, Y. M.; Prior, D. C.; Danielson, W. F.; Belov, M. E.; Smith, R. D. Enhanced Ion Utilization Efficiency Using an Electrodynamic Ion Funnel Trap as an Injection Mechanism for Ion Mobility Spectrometry. *Anal. Chem.* **2008**, *80* (3), 612−623.
(42) Ibrahim, Y. M.; Garimella, S. V. B.; Tolmachev, A. V.; Baker, E. S.; Smith, R. D. Improving Ion Mobility Measurement Sensitivity by Utilizing Helium in an Ion Funnel Trap. *Anal. Chem.* **2014**, *86* (11), 5295−5299.
(43) Ibrahim, Y.; Belov, M. E.; Tolmachev, A. V.; Prior, D. C.; Smith, R. D. Ion Funnel Trap Interface for Orthogonal Time-of-Flight Mass Spectrometry. *Anal. Chem.* **2007**, *79* (20), 7845−7852.
(44) Chouinard, C. D.; Nagy, G.; Webb, I. K.; Garimella, S. V. B.; Baker, E. S.; Ibrahim, Y. M.; Smith, R. D. Rapid Ion Mobility Separations of Bile Acid Isomers Using Cyclodextrin Adducts and Structures for Lossless Ion Manipulations. *Anal. Chem.* **2018**, *90* (18), 11086−11091.
(45) Chouinard, C. D.; Nagy, G.; Webb, I. K.; Shi, T.; Baker, E. S.; Prost, S. A.; Liu, T.; Ibrahim, Y. M.; Smith, R. D. Improved Sensitivity and Separations for Phosphopeptides using Online Liquid Chromotography Coupled with Structures for Lossless Ion Manipulations Ion Mobility−Mass Spectrometry. *Anal. Chem.* **2018**, *90* (18), 10889−10896.
(46) Mariano, A. V.; Su, W.; Guharay, S. K. Effect of Space Charge on Resolving Power and Ion Loss in Ion Mobility Spectrometry. *Anal. Chem.* **2009**, *81* (9), 3385−3391.
(47) Tolmachev, A. V.; Clowers, B. H.; Belov, M. E.; Smith, R. D. Coulombic Effects in Ion Mobility Spectrometry. *Anal. Chem.* **2009**, *81* (12), 4778−4787.
(48) Fernandez de la Mora, J. Space Charge Effects on Ion Mobility Spectrometry. *J. Am. Soc. Mass Spectrom.* **2019**, *30* (6), 1082−1091.
(49) Higuera, F. J.; Fernandez de la Mora, J. The spreading of an axisymmetric ion beam by space charge and diffusion. *J. Aerosol Sci.* **2020**, *147*, 105571.
(50) Eldrid, C.; O'Connor, E.; Thalassinos, K. Concentration-dependent coulombic effects in travelling wave ion mobility spectrometry collision cross section calibration. *Rapid Commun. Mass Spectrom.* **2020**, *34* (S4), No. e8613.
(51) Hong, Y.; Su, J.; Tang, C.; Huang, C.; Liu, S.; Chu, Y. Analysis of the false peaks in extended Hadamard transform ion mobility spectrometry. *Int. J. Mass Spectrom.* **2019**, *446*, 116230.
(52) Xu, J.; Whitten, W. B.; Ramsey, J. M. Space Charge Effects on Resolution in a Miniature Ion Mobility Spectrometer. *Anal. Chem.* **2000**, *72* (23), 5787−5791.
(53) Huntley, A. P.; Hollerbach, A. L.; Prabhakaran, A.; Garimella, S. V. B.; Giberson, C. M.; Norheim, R. V.; Smith, R. D.; Ibrahim, Y. M. Development of a Structure for Lossless Ion Manipulations (SLIM) High Charge Capacity Array of Traps. *Anal. Chem.* **2023**, *95* (9), 4446−4453.
(54) Hoaglund-Hyzer, C. S.; Counterman, A. E.; Clemmer, D. E. Anhydrous protein ions. *Chem. Rev.* **1999**, *99* (10), 3037−3080.
(55) Causon, T. J.; Si-Hung, L.; Newton, K.; Kurulugama, R. T.; Fjeldsted, J.; Hann, S. Fundamental study of ion trapping and multiplexing using drift tube-ion mobility time-of-flight mass spectrometry for non-targeted metabolomics. *Anal. Bioanal. Chem.* **2019**, *411* (24), 6265−6274.
(56) Majima, T.; Santambrogio, G.; Bartels, C.; Terasaki, A.; Kondow, T.; Meinen, J.; Leisner, T. Spatial distribution of ions in a linear octopole radio-frequency ion trap in the space-charge limit. *Phys. Rev. A* **2012**, *85* (5), No. 053414.
(57) Tolmachev, A. V.; Udseth, H. R.; Smith, R. D. Radial stratification of ions as a function of mass to charge ratio in collisional cooling radio frequency multipoles used as ion guides or ion traps. *Rapid Commun. Mass Spectrom.* **2000**, *14* (20), 1907−13.

https://doi.org/10.1021/jasms.3c00389
J. Am. Soc. Mass Spectrom. 2024, 35, 365−377